ACS OMEGA

Article

Cite This: ACS Omega 2019, 4, 11004−11013

http://pubs.acs.org/journal/acsodf

Boosting Upconversion Photoluminescence and Multielectrical Properties via Er-Doping-Modulated Vacancy Control in $Ba_{0.85}Ca_{0.15}Ti_{0.9}Zr_{0.1}O_3$

Chunwen Liu,[†] Quanlin Wang,[†] Xiao Wu,*[,†] Baisheng Sa,*[,†] Hailing Sun,[‡] Laihui Luo,[§] Cong Lin,[†] Xinghua Zheng,[†] Tengfei Lin,[†] and Zhimei Sun[∥]

[†]Key Laboratory of Eco-Materials Advanced Technology, College of Materials Science and Engineering, Fuzhou University, Fuzhou 350108, P. R. China

[‡]Department of Applied Physics, The Hong Kong Polytechnic University, Kowloon, Hong Kong, P. R. China

[§]Department of Microelectronic Science and Engineering, Ningbo University, Ningbo 315211, P. R. China

[∥]School of Materials Science and Engineering and Center for Integrated Computational Materials Science, International Research Institute for Multidisciplinary Science, Beihang University, Beijing 100191, P. R. China

Supporting Information

ABSTRACT: The lead-free $0.5(Ba_{0.7}Ca_{0.3})TiO_3-0.5Ba(Ti_{0.8}Zr_{0.2})O_3$ (BCTZ) ceramics with Er doping have shown good upconversion photoluminescence (PL) and desirable optical temperature sensing properties. To bridge a relationship between the structure/intrinsic defects and properties of rare-earth-doped ferroelectrics, we designed and fabricated a series of BCTZ ceramics doped with 1 mol % Er^{3+} by combining the first-principles calculations and experimental measurements. Theoretically, we discovered that Er can occupy both A sites (i.e., replacing Ba or Ca) and B sites (i.e., replacing Ti or Zr) in the BCTZ lattice and highlighted that the Er-doping-induced vacancy concentration decreases for both the oxygen vacancies (V_o) and cation vacancies (V_c). Experimentally, the enhanced PL performance and the dielectric, ferroelectric, and piezoelectric properties of the Er-doped BCTZ ceramics have been observed. Finally, the physical origin of Er-induced property enhancement in BCTZ has been elaborated according to the charge density and chemical bonding analysis. These results open up a path to investigate the effects of site substitution and vacancies on optoelectronic properties of multifunctional rare-earth-doped ferroelectrics.

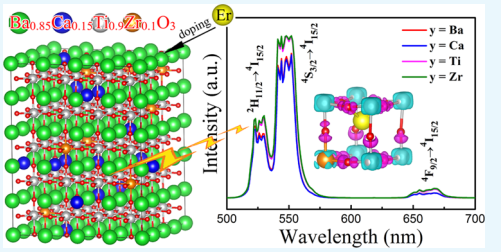

1. INTRODUCTION

Optoelectronic multifunctional materials that own two or more properties in a single entity have emerged as promising next-generation materials for the development of digitization, integration, and miniaturized equipment.[1] Recently, rare-earth ions RE^{3+} (e.g., Pr^{3+}, Er^{3+}, Ho^{3+}, La^{3+}, Eu^{3+})-modified ferroelectrics, one kind of multifunctional optoelectronic materials possessing both photoluminescence (PL) and ferroelectric properties, have been intensively investigated for the application of power generation, data storage, optical telecommunication, and remote sensing.[2−5] Among RE^{3+}, Er^{3+} is an important activator in upconversion luminescence materials, which are attractive in upconversion lasers, planar waveguide, and bioseparation.[6,7] Er-doped ferroelectrics have been verified to be a promising candidate for realizing multifunction; for instance, Er-doped $CaBi_4Ti_4O_{15}$ and Er-doped $(K, Na)NbO_3$ ceramics exhibit bright upconversion emission and superior piezoelectric/ferroelectric properties.[1,8]

A suitable host that matches well with Er^{3+} is required for Er-doped ferroelectrics to achieve excellent multifunctionality. Traditional lead-based ferroelectric hosts cannot realize long-term functionality with a view to protect environmental and human health. Recently, a breakthrough was obtained by Liu and Ren in the lead-free system, $0.5(Ba_{0.7}Ca_{0.3})TiO_3-0.5Ba(Ti_{0.8}Zr_{0.2})O_3$ (BCTZ) ceramics, which possesses an ultrahigh piezoelectric coefficient ($d_{33} \approx 620$ pC/N) and is comparable to the lead-based (Pb, Zr)TiO_3 piezoelectric ceramics.[9] The distinctive piezoelectric response of BCTZ originates from the coexistence of multiphase near morphotropic phase boundary, such as rhombohedral−tetragonal (R−T) phases or rhombohedral−orthonormal−tetragonal phases.[9,10] Besides, good upconversion PL and desirable optical temperature sensing properties have been obtained in Er-doped BCTZ ceramics for optical applications.[11] However, the relationship between structure/intrinsic defects and properties in BCTZ-based materials has not been explored thoroughly.

Furthermore, the PL properties of Er^{3+} in Er-doped ferroelectrics are closely related to the crystal field, which is

Received: May 14, 2019
Accepted: June 12, 2019
Published: June 24, 2019

DOI: 10.1021/acsomega.9b01391
ACS Omega 2019, 4, 11004−11013

determined by the crystal symmetry (phase structure) and chemical environment (e.g., point defects such as vacancies) of the host. However, Er^{3+} cannot substitute for a single site in BCTZ and the induced vacancies are uncertain, increasing the complexity for studying the intrinsic effect on properties.[12] Additionally, density functional theory (DFT) calculation is a powerful tool to explain the microscopic mechanisms of spontaneous polarization, energetics, and phase diagrams in ferroelectrics, which can be used to combine with experimental results for elaborating the mechanism.[13−15] The dominant native point defects in the ABO_3 structure are expected to be vacancies, which constantly influence the physical properties, e.g., piezoelectricity and ferroelectricity.[16] From this concern, a detailed understanding of the effect of structure and vacancies on the optoelectronic properties of Er-doped BCTZ is vital in extending the optoelectronic multifunctional applications.

In this work, we designed a series of BCTZ ceramics doped with 1 mol % Er^{3+}, combining with solid-state reaction synthesis and the first-principles calculations. The generated oxygen vacancies (V_o) and cation vacancies (V_c) and the effect of vacancies on PL performance, dielectric, ferroelectric, and piezoelectric properties of the ceramics have been further investigated. The physical origin of Er-induced changes in PL, ferroelectric, and piezoelectric properties of BCTZ has been unraveled based on the first-principles calculations as well. The A-site doping of Er in BCTZ brings local distortions along the ⟨001⟩ direction, resulting in dual-enhancement in PL and piezoelectric properties.

2. FIRST-PRINCIPLES CALCULATIONS AND EXPERIMENTAL

Our DFT calculations were performed by the GPU-accelerated Vienna ab initio simulation package[17,18] in conjunction with the projector augmented wave generalized gradient approximations[19] (GGAs) of Perdew−Burke−Ernzerhof[20] (PBE) pseudopotentials. The valence electron configurations for Ba, Ca, Ti, Zr, Er, and O were $5s^25p^66s^2$, $3p^64s^2$, $4s^23d^2$, $4s^24p^65s^24d^2$, $5p^64f^16s^2$, and $2s^22p^4$, respectively. We used a $4 \times 4 \times 5$ T phase BCTZ supercell including 400 atoms and Γ symmetry K-point set for all of the calculations. The relaxation convergences for ions and electrons were 1×10^{-5} and 1×10^{-6} eV, respectively, which were achieved with the cutoff energy of 600 eV. The crystal structures and isosurfaces were visualized by using the VESTA[21] package.

In the experimental process, $Ba_{0.85}Ca_{0.15}Ti_{0.9}Zr_{0.1}O_3$ substituted with x mol % (x = 1) Er^{3+} at A sites (including Ba and Ca in the lattice) and B sites (including Ti and Zr in the lattice) in BCTZ, i.e., $Ba_{0.85-1.5x}Er_xCa_{0.15}Ti_{0.9}Zr_{0.1}O_3$ (substituting Ba by Er), $Ba_{0.85}Ca_{0.15-1.5x}Er_xTi_{0.9}Zr_{0.1}O_3$ (substituting Ca by Er), $Ba_{0.85}Ca_{0.15}Ti_{0.9-x}Er_xZr_{0.1}O_{3-0.5x}$ (substituting Ti by Er), and $Ba_{0.85}Ca_{0.15}Ti_{0.9}Zr_{0.1-x}Er_xO_{3-0.5x}$ (substituting Zr by Er), were fabricated by the conventional solid-state reaction technique. High-purity powders $BaCO_3$ (99.95%), $CaCO_3$ (99.99%), TiO_2 (99.99%), ZrO_2 (99.99%), and Er_2O_3 (99.9%) were used as the starting materials. The powders in the stoichiometric ratio were ball-milled thoroughly in an alcohol by agate balls for 12 h and then dried and calcined at 1200 °C for 2 h in air before second ball milling for 12 h. After sieving through an 80 mesh screen and mixing with 5 wt % poly(vinyl alcohol) binder solution, the resulting mixture was pressed into pellets, followed by burning out the binder at 800 °C for 2 h. Finally, the disk samples were sintered at 1440 °C in air for 2 h to obtain ceramics. Before electrical measurement, silver electrodes were coated on both surfaces of ceramics. Then, the ceramics were poled under a 2 kV/mm electric field in silicone oil at room temperature for 15 min.

The phase structure of ceramics were checked using an X-ray diffraction (XRD) analyzer (Rigaku Ultima III) with Cu $K\alpha$ radiation. The morphology of samples was investigated using a field-emission scanning electron microscope (FESEM, Zeiss Supra 55). The piezoelectric coefficient d_{33} and polarization−electric field (P−E) loops of ceramics were measured by a quasi-static piezoelectric meter (YE2730-A, Sinocera Piezotronics, Inc.) and a ferroelectric test system (TF Analyzer 2000, aixACCT), respectively. The room-temperature dielectric constant, ε_r, and dielectric loss, tan δ, at 10 kHz were measured using an impedance analyzer (HP 4294 A, Agilent Technologies, Inc., Palo Alto, CA). The Raman spectra were obtained using a grating spectrometer (HORIBA Jobin Yvon, HR800) equipped with a 488 nm-line laser as the excitation source. The photoluminescence properties of ceramics were recorded at room temperature by a 980 nm laser using a spectrofluorometer (Ocean Optics USB4000).

3. RESULTS AND DISCUSSION

Our design principle was to optimize the thermodynamic driving force and find the favorable doping positions for Er in the BCTZ crystal lattice. We also desire a deeper understanding of the relationship between the Er dopant and induced intrinsic vacancies. Our DFT calculations were based on a $4 \times 4 \times 5$ supercell from the T-phase ABO_3 unit cell by including the special quasi-random structure (SQS) approach,[22] which can closely mimic the most relevant local pair and multisite correlation functions of the random occupations. To represent the stoichiometric ratio of 0.5-$(Ba_{0.7}Ca_{0.3})TiO_3$−0.5$Ba(Zr_{0.2}Ti_{0.8})O_3$, the A-site atoms of our model includes 68 Ba atoms and 12 Ca atoms and the B-site atoms includes 72 Ti atoms and 8 Zr atoms. Figure 1a illustrates the SQS structure of the BCTZ supercell. The fully relaxed lattice parameters a and c are 4.034 and 4.087 Å, respectively. More details of the SQS structure of the BCTZ supercell are presented in the Supporting Information.

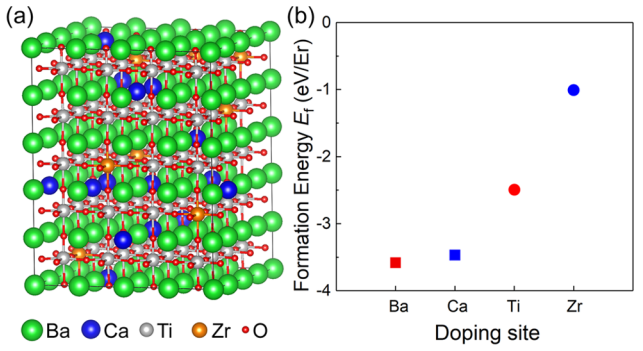

Figure 1. (a) SQS structure of the BCTZ $4 \times 4 \times 5$ supercell including 400 atoms. (b) Formation energy of Er-doped BCTZ with different Er-doping sites.

To unravel the chemical driving force of Er dopant in BCTZ, we replaced one metallic cation site by one Er atom to achieve the 1.25% Er-doping concentration. The formation energy, E_f, of the corresponding Er dopant is calculated as follows

DOI: 10.1021/acsomega.9b01391
ACS Omega 2019, 4, 11004−11013

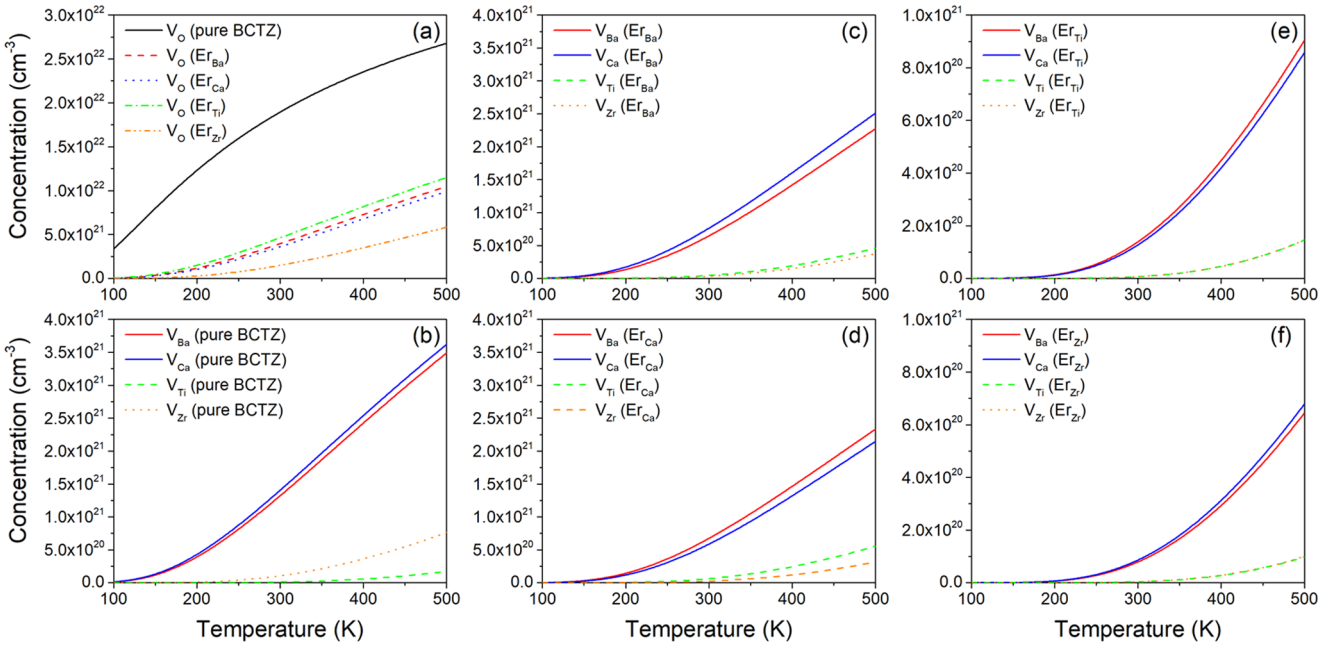

Figure 2. Concentration of various defects as a function of temperature for (a) V_o and (b)−(f) V_c in BCTZ.

$$E_f = E_{total}^{Er:BCTZ} - E_{total}^{BCTZ} + n\mu_x - n\mu_{Er} \quad (1)$$

where E_{total}^{BCTZ} and $E_{total}^{Er:BCTZ}$ are the total energies of the pure and Er-doped BCTZ, respectively, and μ_{Er} and μ_x are the chemical potentials of solid ground-state Er and Ba/Ca/Ti/Zr, respectively, and n = 1 for one Er dopant. Figure 1b presents the calculated formation energy of Er-doped BCTZ with different Er-doping sites. The negative value of the formation energy indicates that the Er-doping process is an exothermic reaction for all of the cation sites. As a result, the Er dopants can replace both A and B sites in BCTZ regardless of designed site substitutions by Er. On the other hand, the formation energy follows the sequence of $Er_{Zr} > Er_{Ti} > Er_{Ca} \approx Er_{Ba}$, suggesting that A-site doping is more energetically favorable than B-site doping. Hence, we assume that the Er dopant mainly occupies the A site by replacing the Ba or Ca atoms and partly occupies the B site by replacing the Ti or Zr atoms.

To get further understanding of the defects in BCTZ, we predicted the equilibrium defect concentrations, [D], based on the defect formation energies, H_f, by[23]

$$[D] = N_{sites} \exp\left(-\frac{H_f}{K_B T}\right) \quad (2)$$

$$H_f = E_{defect}^{BCTZ} - E_{no\text{-}defect}^{BCTZ} + \mu_d \quad (3)$$

where N_{sites} is the number of sites per unit volume of BCTZ where the defects may be present, K_B and T are the Boltzmann constant and temperature, respectively, E_{defect}^{BCTZ} and $E_{no\text{-}defect}^{BCTZ}$ are the total energies of BCTZ with and without defects, respectively, and μ_d is the chemical potential of solid ground-state defect matter.

Figure 2a shows the V_o concentration in BCTZ under different chemical environments. It is interesting to find that the Er doping can significantly reduce the V_o concentration in BCTZ. For instance, the V_o concentration is about 2.0×10^{22} cm^{-3} for pure BCTZ at 300 K, which reduces to less than 5.0×10^{21} cm^{-3} for Er-doped BCTZ regardless of the doping sites. Considering the fact that the dipole polarization of BCTZ ceramics is sensitive to the V_o concentration, distinguished electrical properties of Er-doped BCTZ ceramics are anticipated.

On the other hand, Figure 2b illustrates the concentrations of different V_c (including V_{Ba}, V_{Ca}, V_{Ti}, and V_{Zr}) in BCTZ and Figure 2c−f illustrates the corresponding vacancies after Er doping. Some interesting conclusions can be obtained herein: (1) the V_c concentration is much lower than V_o in pure BCTZ. (2) The concentration of A-site vacancies is much higher than that of B-site vacancies; for instance, the concentrations of V_{Ba} and V_{Ca} are 1.3×10^{21} and 1.4×10^{21} cm^{-3} for pure BCTZ at 300 K, respectively, whereas the concentrations of V_{Ti} and V_{Zr} are 8.9×10^{18} cm^{-3} and 1.0×10^{20} cm^{-3} for pure BCTZ at 300 K, respectively. (3) The Er dopant at A site can only slightly reduce the V_c concentration in BCTZ, while the Er dopant at B site can significantly reduce the V_c concentration in BCTZ. All in all, the Er-doped BCTZ ceramics include less vacancies than the pure BCTZ both in the oxygen and cation sites. The computational results indicate that Er-doped BCTZ deserved experimental investigations.

The ceramic samples are abbreviated as BCTZ-Er-y (y = 0, Ba, Ca, Ti, or Zr), where y corresponds to different synthesized chemical environments. Herein, for y = 0, $BaCO_3$, $CaCO_3$, TiO_2, and ZrO_2 follow the stoichiometric ratio of BCTZ (i.e., $0.5(Ba_{0.7}Ca_{0.3})TiO_3 - 0.5Ba(Zr_{0.2}Ti_{0.8})O_3$ or $Ba_{0.85}Ca_{0.15}Ti_{0.9}Zr_{0.1}O_3$) without adding any Er_2O_3. For y = Ba/Ca/Ti/Zr, we included 0.5% molar concentration Er_2O_3 and reduced 1% molar concentration $BaCO_3/CaCO_3/TiO_2/ZrO_2$ in the stoichiometric ratio of BCTZ, respectively.

The XRD patterns of the BCTZ-Er-y ceramics are shown in Figure 3a. All of the obtained ceramics possess perovskite structure, and there is no trace of secondary phases. T phase is dominant in the ceramics, which can be evidenced by the splitting of the (001)/(100) and (002)/(200) peaks (Figure 3b,d).[24] Compared with the pure BCTZ (i.e., y = 0), the splitting of these diffraction peaks become more obvious after introducing Er^{3+}, suggesting that the content of T phase increases in BCTZ-Er-y ceramics. It is interesting to note that

DOI: 10.1021/acsomega.9b01391
ACS Omega 2019, 4, 11004−11013

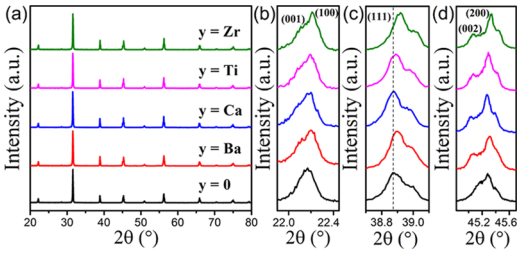

Figure 3. (a) XRD patterns of BCTZ-Er-*y* ceramics and (b–d) zoomed XRD patterns at 2θ of 22.2°, 38.8°, 45.2°, respectively.

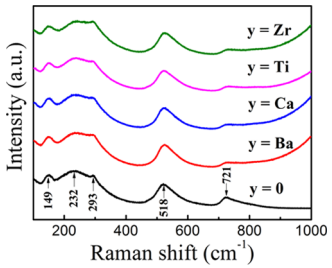

Figure 4. Raman spectra of BCTZ-Er-*y* ceramics.

our designed chemical environment is not directly related to the doping site of Er^{3+}. The (111) diffraction peaks around 38.8° of the ceramics with *y* = Ti and Zr (Figure 3c) shift toward higher angles compared to those with *y* = 0. That should be attributed to the substitution of A-site ions Ba^{2+} (0.161 nm, coordination number CN = 12) and Ca^{2+} (0.134 nm, CN = 12) with smaller Er^{3+} (0.122 nm, CN = 12), resulting in lattice shrinkage and simultaneous generation of V_c. While for the ceramics with *y* = Ba and *y* = Ca, some Er^{3+} substitute for the A site (similar to *y* = Ti and *y* = Zr) but other Er^{3+} (0.089 nm, CN = 6) incorporate into smaller B-site ions, i.e., Ti^{4+} (0.0605 nm, CN = 6) and Zr^{4+} (0.072 nm, CN = 6), leading to lattice expansion and producing V_o. No notable shift of the (111) diffraction peak can be observed in BCTZ-Er-Ca (Figure 3c), indicating that both A and B sites have been occupied by Er^{3+} and the amounts of individual replacement are close.

To further investigate the lattice parameters of the BCTZ-Er-*y* ceramics, a general diffraction analysis program was performed using the Rietveld method by considering the *P4mm* space group of $BaTiO_3$ (Figure S1). According to the designed chemical formula, Ba was replaced by Ca and Ti was replaced by Zr for the refinements. Table S1 gives the refined structural parameters, i.e., lattice parameters (*a*, *b*, *c*, and β), calculated tetragonality ratio (*c*/*a*), as well as the reliability factors (R_{wp}) and goodness-of-fit indicators (*S*). The low R_{wp} (<15%) and *S* (<2) values manifest good fits between the observed and calculated patterns. Comparing to the DFT data, we found that the experimental measured data are slightly smaller than the computational predicted ones. This is due to the fact that GGA-PBE pseudopotential always overestimates the lattice parameters.[25] It is worth noting that the BCTZ-Er-*y* ceramics show lower R_{wp} values than pure BCTZ ceramics, indicating that Er doping do reduce the concentration of oxygen vacancies or cation vacancies in BCTZ. As given in Table S1, the lattice parameters (*a*, *b*, and *c*) of BCTZ-Er-*y* (*y* = Ti, Zr) are smaller than those of BCTZ-Er-*y* (*y* = Ba, Ca), suggesting that more Er^{3+} substitute for the A site at *y* = Ti and *y* = Zr. Compared to those of pure BCTZ (*y* = 0), the *c*/*a* values of BCTZ-Er-*y* (*y* = Ba, Ca, Ti, Zr) are all larger because their T phases are predominant.

The Raman spectra of the BCTZ-Er-*y* ceramics are shown in Figure 4. It is known that the cubic $BaTiO_3$ owns 15 degrees of freedom for vibration, consisting of triply degenerate acoustic mode (one F_{1u}) and optical modes (three F_{1u} and one F_{2u}).[26] While in the tetragonal $BaTiO_3$, owing to the polarization between Ti^{4+} and O^{2-}, the F_{1u} mode splits into three A_1 modes and three E modes, and the F_{2u} mode splits into B_1 and E mode. Thus, the Raman-active optical lattice vibration of T-phase $BaTiO_3$ can be expressed as $3A_1 + B_1 + 4E$.[27] Furthermore, A_1 and E optical modes are separated into transversal (TO) and longitudinal (LO) components because of long-range electrostatic forces from the ions in crystal lattice.[26] The Raman bands (Figure 4) at 232, 518, 293, and 721 cm^{-1} confirm that T phase is dominating in the ceramics,[28] which is in consistent with the XRD results. The bands at 232 and 518 cm^{-1} correspond to A_1(TO) character and the 232 cm^{-1} one is especially related to polar Ti–O vibration. These very similar peaks of all our samples confirm the stability of the T phase. On the other hand, the bands at 293 cm^{-1} (B_1 and E(TO + LO) modes) are assigned to the asymmetry within the $[TiO_6]/[ZrO_6]$ octahedral and the bands at 721 cm^{-1} (mixing with A_1 and E modes) are designated to the bending or stretching of $[TiO_6]/[ZrO_6]$ octahedral in the BCTZ-Er-*y* ceramics.[29,30] We found that after doping with Er these two bands become broader with weaker intensities, indicating that Er doping may reduce the integrity and symmetry in BCTZ ceramics.

Figure 5 shows the surface morphologies of the BCTZ-Er-*y* ceramics. All of the specimens exhibit dense microstructures with the relative densities of > 95% (as given in Table 1) and the mean grain sizes of 21.38 μm (*y* = 0), 7.33 μm (*y* = Ba), 6.77 μm (*y* = Ca), 8.88 μm (*y* = Ti), and 7.52 μm (*y* = Zr). It is interesting to find that the grain size decreases after the inclusion of the Er dopant into the BCTZ ceramics. Based on our calculation, Er^{3+} ions preferentially occupy the A site by substituting for Ba^{2+} or Ca^{2+} regardless of designed replacing sites for Er^{3+}; thus, the donor-type nature of Er^{3+} in BCTZ will be expressed. Then, the donor-doping ions induced vacancies concentrate near the grain boundaries, hindering their mobility during densification and ultimately inhibiting the grain growth of ceramics.[31] More importantly, Er doping is propitious to increasing the relative density of the BCTZ ceramics. For instance, the relative density of pure BCTZ (for *y* = 0) is 95.76%, which increases to the highest value of 97.69% for *y* = Ti. Higher relative densities indicate lower concentration of vacancies after Er doping, which agrees well with our calculation and XRD results. Compared to those in BCTZ-Er-*y* (*y* = Ba, Ca) ceramics, the BCTZ-Er-*y* (*y* = Ti, Zr) ones possess less pores with higher relative densities, suggesting that the BCTZ-Er-*y* (*y* = Ti, Zr) samples may exhibit better properties. To confirm the existence and distribution of Ba, Ca, Ti, Zr, Er, and O elements, elemental mappings are performed for the ceramics (Figure S2), testifying that all of the elements are homogeneously distributed in the BCTZ host.

Figure 6 shows the temperature dependence of dielectric properties of the BCTZ-Er-*y* ceramics. For pure BCTZ, two dielectric anomalies centered at approximately 48 and 95 °C can be detected, corresponding to the rhombohedral–tetragonal and tetragonal-cubic phase transition temperatures (T_{R-T} and T_c), respectively. As the two dielectric peaks diffuse, phase transitions in pure BCTZ take place in a temperature

DOI: 10.1021/acsomega.9b01391
ACS Omega 2019, 4, 11004–11013

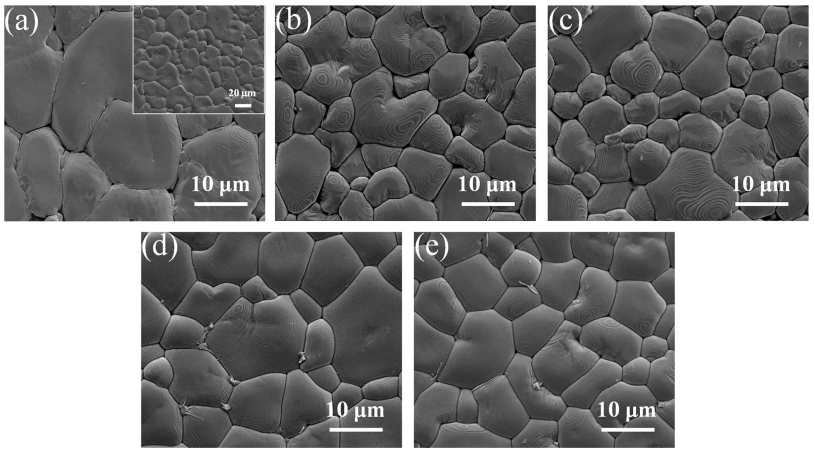

Figure 5. SEM micrograph of surface morphologies of BCTZ-Er-*y*: (a) $y = 0$, (b) y = Ba, (c) y = Ca, (d) y = Ti, (e) y = Zr.

Table 1. Mean Grain Sizes and Relative Densities of BCTZ-Er-*y* Ceramics

y	0	Ba	Ca	Ti	Zr
grain size (μm)	21.38	7.33	6.77	8.88	7.52
relative density (%)	95.76	96.65	96.72	97.69	97.62

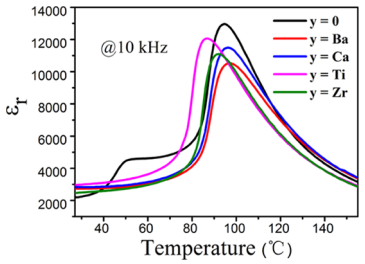

Figure 6. Temperature dependence of dielectric properties of BCTZ-Er-*y* ceramics.

range rather than a fixed temperature. It is possible that R and T phases coexist at room temperature as the first central phase transition temperature (i.e., 48 °C) is close to room temperature, whereas for the Er-doped BCTZ ceramics, only one dielectric anomaly (corresponding to T_c) can be observed at 96, 97, 86, and 91 °C for y = Ba, Ca, Ti, and Zr, respectively, manifesting that only tetragonal phase exists at room temperature. The results are consistent with the XRD analysis. In addition, vacancies in the dielectric ceramics can influence T_c; for instance, T_c decreases after the introduction of V_c.[32,33] Hence, compared with the ceramics with $y = 0$, Ba, and Ca, the V_c concentrations of ceramics with y = Ti and y = Zr are higher and the effect on reducing T_c is dominant.

The PL properties of the BCTZ-Er-*y* ceramics were examined, as shown in Figure 7. The upconversion PL emission spectra (Figure 7a) manifest that under the excitation of 980 nm there are two strong green emission bands and one weak red emission band locating at ~522, 550, and 667 nm, resulting from the $^2H_{11/2} \rightarrow {}^4I_{15/2}$, $^4S_{3/2} \rightarrow {}^4I_{15/2}$, and $^4F_{9/2} \rightarrow {}^4I_{15/2}$ transitions of Er^{3+}, respectively. A clear splitting of emission peaks can be observed, ascribed to the Stark splitting of the degenerate 4f levels of Er^{3+} under strong crystal field,[34] which is affected by the interaction between Er^{3+} and the BCTZ host. The PL intensities of BCTZ-Er-*y* (y = Ba, Ca) are weaker than those of BCTZ-Er-*y* (y = Ti, Zr). It is known that the emission of Er^{3+} in luminescent materials can be quenched by a small amount of V_o because the positive charge of V_o can

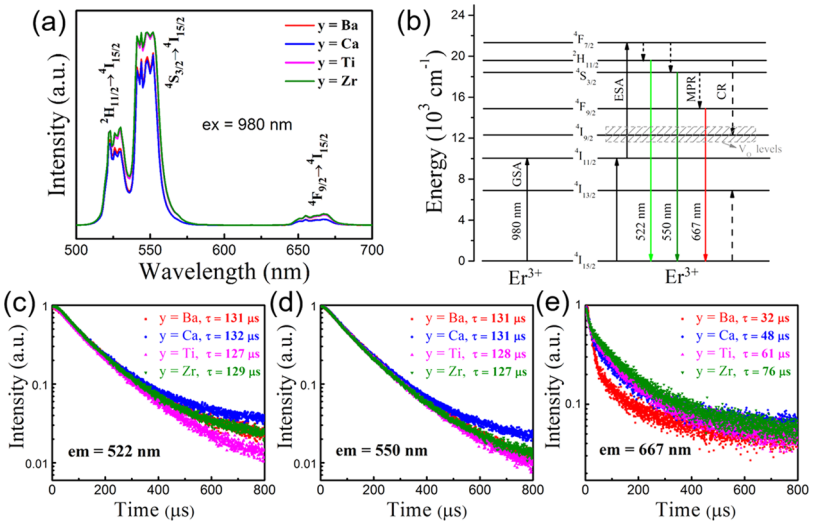

Figure 7. (a) Upconversion PL spectra of BCTZ-Er-*y* ceramics. (b) Schematic diagram for the upconversion mechanism of Er^{3+} under the excitation of 980 nm. (c)−(e) PL decay curves monitoring the emissions at (c) 522 nm, (d) 550 nm, and (e) 667 nm.

DOI: 10.1021/acsomega.9b01391
ACS Omega 2019, 4, 11004−11013

trap the excited electrons to reduce the photons used for radiative emission.[35] On the other hand, structural symmetry and density of ceramics play an important role in the PL intensity. Compared to those of BCTZ-Er-y (y = Ba, Ca), BCTZ-Er-y (y = Ti, Zr) exhibit lower symmetries (slightly higher c/a values as listed in Table S1), higher relative densities (Table 1), and fine grains, contributing to the enhancement of PL intensities.

The decay curves from the upconversion emissions at 522 nm ($^2H_{11/2} \rightarrow {}^4I_{15/2}$), 550 nm ($^4S_{3/2} \rightarrow {}^4I_{15/2}$), and 667 nm ($^4F_{9/2} \rightarrow {}^4I_{15/2}$) of the BCTZ-Er-$y$ ceramics are shown in Figure 7c–e. Because of the energy transfer during the upconversion process, the decay exhibits slight nonexponential curves, which can be fitted by the following equation

$$\tau = \frac{\int_0^\infty I(t)t\,dt}{\int_0^\infty I(t)\,dt} \quad (4)$$

where $I(t)$ represents the PL intensity at a time t after the cutoff of 980 nm excitation and τ is the PL lifetime. For the two green emission bands at 522 and 550 nm, the calculated lifetimes of the ceramics are all close to 130 μs (Figure 7c,d), indicating that upconversion green emission bands are almost independent of host symmetry and internal defects. However, the vacancies in the ceramics significantly influence the PL lifetime of red emission at 667 nm. It is reported that in Er-doped perovskite titanate V_o in the material can greatly reduce the PL lifetime.[36] Therefore, the ceramics with y = Ba and Ca that contain more V_o have shorter lifetimes than those of y = Ti and Zr (Figure 7e). Among them, the lifetime of red emission of BCTZ-Er-Zr is the longest (76 μs). Cation vacancies, V_c, acting as a nonradiative recombination center,[37,38] can increase the probability of cross relaxation (CR) and then decrease the PL lifetime. Nevertheless, the effect of V_c on CR of the BCTZ-Er-y ceramics is unobvious because the concentration of Er^{3+} is low (only 1 mol %).

For further studying the vacancy effect on PL intensity and lifetime, the upconversion PL mechanism is requisite to be discussed based on the energy-level diagram of Er^{3+}, as shown in Figure 7b. Under the excitation of 980 nm, Er^{3+} can populate the $^4F_{7/2}$ level via the ground-state absorption (GSA) and excited-state absorption (ESA). Then, multiphonon relaxation occurs and Er^{3+} ions relax nonradiatively to $^2H_{11/2}$, $^4S_{3/2}$, and $^4F_{9/2}$ levels subsequently, producing the green $^2H_{11/2}/{}^4S_{3/2} \rightarrow {}^4I_{15/2}$ and red $^4F_{9/2} \rightarrow {}^4I_{15/2}$ emission spectra. The energy level of V_o should reside above the $^4I_{11/2}$ level of Er^{3+}, which is similar to that in Er-doped $0.93Bi_{0.5}Na_{0.5}TiO_3$–$0.07BaTiO_3$.[39] In the ceramics with y = Ba and Ca, more V_o can trap excited electrons used for ESA and radiative emissions during the upconversion process, thus reducing the populations of the $^4F_{7/2}$, $^2H_{11/2}$, $^4S_{3/2}$, and $^4F_{9/2}$ levels and then decreasing the green and red emission spectra (Figure 7a). Also, the presence of V_o would induce new energy levels above $^4I_{11/2}$ to enhance the nonradiative energy transfer,[36] decreasing the population of the $^4F_{9/2}$ level (close to the V_o levels) and then the PL lifetimes at 667 nm.

The ferroelectric P–E hysteresis loops of the BCTZ-Er-y ceramics are shown in Figure 8. The pure BCTZ exhibits a slim loop with a large remanent polarization (P_r = 13.8 μC/cm^2) and a low coercive field (E_c = 0.98 kV/mm), as listed in Table 2. Due to the disruption of long-range ferroelectric order[40] induced by Er doping and the inhibition of domain-wall

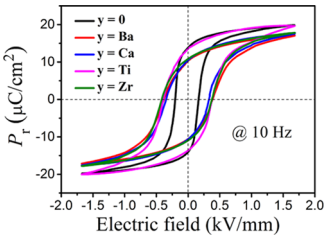

Figure 8. P–E hysteresis loops of BCTZ-Er-y ceramics.

Table 2. Ferroelectric and Piezoelectric Properties of BCTZ-Er-y Ceramics

y	d_{33} (pC/N)	P_r (μC/cm^2)	E_c (kV/mm)
0	270	13.8	0.17
Ba	225	10.3	0.39
Ca	255	10.4	0.33
Ti	372	13.6	0.38
Zr	330	10.8	0.38

movement in smaller grains (Figure 5),[41] the ferroelectric properties of the BCTZ-Er-y ceramics exhibit deterioration with smaller P_r and larger E_c. In addition, Er doping significantly affects the piezoelectric performance of the ceramics. The BCTZ-Er-y (y = Ti, Zr) ceramics possess larger d_{33} (372 and 330 pC/N) than that of pure BCTZ (d_{33} = 270 pC/N), while the BCTZ-Er-y (y = Ba, Ca) ones have smallest d_{33} (Table 2). The ferroelectric and piezoelectric properties are partly related to vacancies such as V_o and V_c.[42] In BCTZ-Er-y (y = Ba, Ca), more V_o (compared to y = Ti/Zr) can act as space charge to cause strong domain pinning,[43] resulting in increasing E_c and decreasing d_{33}, whereas in BCTZ-Er-y (y = Ti, Zr), abundant V_c can compensate charge disorder and make the domain motion easier, benefiting in enhancing d_{33}.[44,45] The ceramics owning better piezoelectric performance usually possess denser microstructures and higher relative densities. Therefore, the variation tendencies of electrical properties coincide with the SEM analysis (Table 1).

First-principles calculations were performed to further unravel the physical origin of the improved PL and piezoelectric properties of the BCTZ-Er-y ceramics. First, we plotted the total and partial radial distribute function (RDF) for pure BCTZ from our SQS model in Figures S3 and 9a, respectively. The long-range order feature in the SQS model is well represented. More importantly, it is interesting to find that the first RDF peak is contributed by the nearest-neighbored B–O (Ti–O and Zr–O) pair and the second RDF peak is contributed by the nearest-neighbored A–O (Ba–O and Ca–O) pair. Figure 9b further illustrates the cation–O interatomic distances in pure BCTZ. We found that the A-site cation and O are bonded around 2.8–2.9 Å, whereas the B-site cation and O are bonded around 1.9–2.1 Å. Herein, the Ti–O (or Ca–O) bonds are distributed in a wider range than the Zr–O (or Ba–O) bonds. It is understandable because the A-site cations own larger ionic radii than the B-site cations. Figure 9b presents the Er–O interatomic distances for different doping sites in Er-doped BCTZ. The A-site and B-site doping show quite different Er–O interatomic distance distributions. For the A-site doping cases, both the Er_{Ba}–O and Er_{Ca}–O interatomic distances distribute in a very wide range from 2.1 to 3.6 Å. It is interesting to find that the Er_{Ba}–O interatomic distances can be divided to three groups: the B-

DOI: 10.1021/acsomega.9b01391
ACS Omega 2019, 4, 11004–11013

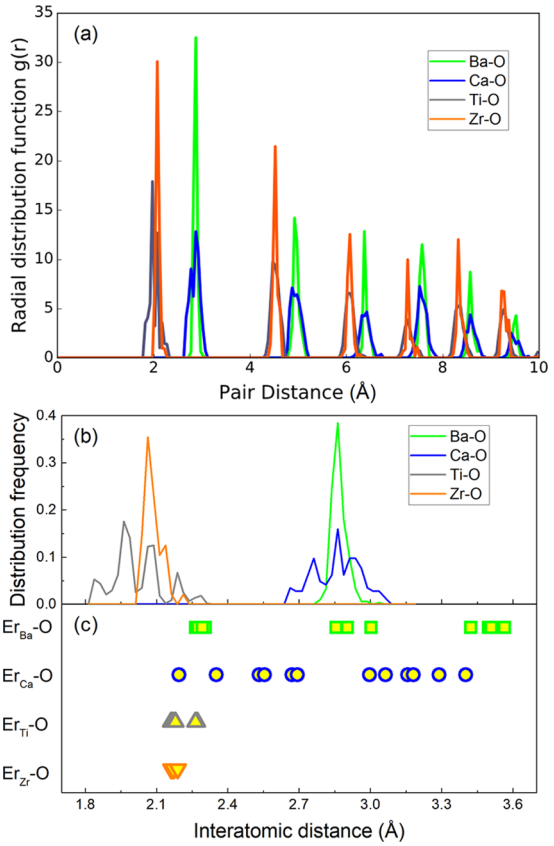

Figure 9. (a) Bond length distribution in pure BCTZ. (b) Er−O bond length in Er-doped BCTZ. (c) Er−O bond length in Er-doped BCTZ.

site-O-like bonding states around 2.25 Å, the A-site-O-like bonding states around 2.8−3.0 Å, and no bonding states around 3.4−3.6 Å. For the B-site doping cases, all of the Er_{Ti}−O and Er_{Zr}−O interatomic distances distribute in very narrow range around 2.2 Å. For a deeper understanding of the cation−O bonding features, we studied the charge transfer from the cation atom to the surrounding O atoms by analyzing the

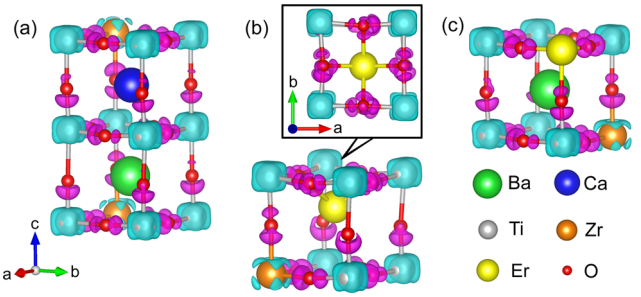

Figure 10. Plots of charge density difference (violet, charge accumulation; cyan, charge depletion) for (a) pure BCTZ, (b) Er_{Ba}-doped BCTZ, and (c) Er_{Zr}-doped BCTZ.

charge density differences, ρ_{diff}, in Figure 10, which are obtained using

$$\rho_{diff} = \rho_{scf} - \rho_{nscf} \quad (5)$$

where ρ_{scf} and ρ_{nscf} correspond to the self-consistent and non-self-consistent charge densities, respectively. The violet isosurfaces denote the charge accumulation ($\rho_{diff} > 0$), and the cyan isosurfaces indicate the charge depletion ($\rho_{diff} < 0$). According to Figure 10a, in pure BCTZ, hexahedron charge depletions of the B-site cations are vividly shown, resulting from the $[TiO_6]$/$[ZrO_6]$ octahedrons in the BCTZ crystal framework. The B-site-O bonds (Ti−O and Zr−O bonds) along the ⟨100⟩ and ⟨010⟩ directions and the Zr−O bonds along the ⟨001⟩ direction can be distinguished by the noticeable charge accumulations at the Ti−O/Zr−O bond center between Ti/Zr and O. Meanwhile, the alternative set of remarkable and negligible charge accumulations of the Ti−O−Ti bonds along the ⟨001⟩ direction show typical alternatively strong and weak Ti−O bond features. Such bonding features explain why we have got the wider Ti−O bond length distribution than Zr−O, as shown in Figure 10a. However, there is no noticeable charge accumulation between the A-site cation (Ba or Ca) and O, indicating that the direct interactions between Ba/Ca and O are very weak in BCTZ. As the A-site cations locate at the center of the octahedral void among the $[TiO_6]$/$[ZrO_6]$ octahedral crystal framework, the crystal field effect are from the interaction between the Ba/Ca atom and $[TiO_6]$/$[ZrO_6]$ octahedrons. As shown in Figure 10b, the Er_{Ba} dopant shifts up from the center of the octahedral void along the ⟨001⟩ direction. As a result, one Er cation will be strongly bonded to four O anions with remarkable charge accumulations at the Er−O bond center between Er and O. Herein, direct interactions between Er and O can be verified. On the other hand, there is no noticeable charge accumulation between Er and the other eight nearest O anions. The coexistence of both strong and weak Er−O interactions will lead to local distortions along the ⟨001⟩ direction in BCTZ. In Figure 10c, we found that the Er_{Zr} dopant plays a very similar role to the Zr cation in BCTZ, where all of the Er−O bonds can be distinguished by the noticeable charge accumulations. To conclude, the A-site doping of Er in BCTZ results in local distortions along the ⟨001⟩ direction, which not only increases the c/a ratio of BCTZ (Table S1) but also increases the PL and piezoelectric properties. Hence, higher PL intensities and larger d_{33} of the ceramics with y = Ti and Zr (compared to y = Ba and Ca) are consistent with our calculations.

A deeper understanding on the chemical bonding nature of Er-doped BCTZ can be gained by analyzing the electron localization function (ELF),[46] which can give a rather quantitative picture on the chemical bonding of compounds. The ELF contours on the (101) plane for pure BCTZ are shown in Figure 11a,b, which give the clear pictures of typical ionic bonding feature of BCTZ by the strong spherical shaped localized electrons around the O atoms. On the other hand, the localized electron states around the Ba and Zr atoms come from the inner-level $5s^25p^6$ and $4s^24p^6$ electrons, respectively. To further understand the chemical bonding characters of BCTZ, we studied the bond point of the cation−O bond by the one-dimensional (1D) line plots of ELF, as marked in the figures. Herein, the bond point is the saddle point in the electron charge with two negative eigenvalues and one positive eigenvalue of the Hessian matrix of ELF.[47] The minimum ELF value in the middle of the curve corresponds to the bond point, and larger bond point value corresponds to the stronger bond interactions.[48] Although we cannot get the bond point for Ti−O, since there are no localized electrons around the Ti atoms, we can still find that the B-site-cation−O bonds are stronger than the A-site-cation−O bonds. The results agree well with our previous analysis about bond length and charge density

DOI: 10.1021/acsomega.9b01391
ACS Omega 2019, 4, 11004−11013

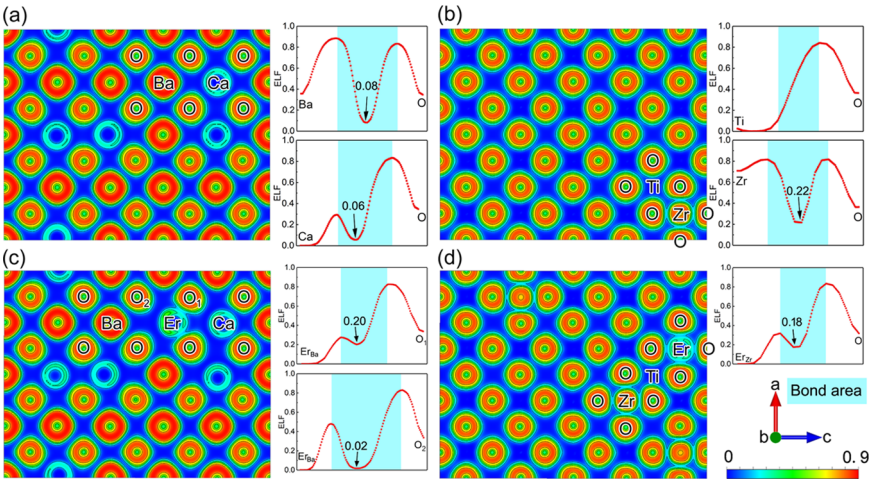

Figure 11. Two-dimensional plane plots and 1D line plots of ELF in (a), (b) pure BCTZ, (c) Er_{Ba}-doped BCTZ, and (d) Er_{Zr}-doped BCTZ. All of the graphs are under the same saturation levels, and the interval between the contour lines is 0.15. The color scale for the ELF value is given at the bottom right of the figure.

difference. As seen from Figure 11c,d, after Er doping, the bond points for $Er_{Ba}-O_1$ and $Er_{Zr}-O$ are 0.20 and 0.18, respectively. These values are very close to the Zr−O bond point in BCTZ, indicating that the Er−O bonds show very similar feature to the Zr−O bond. It is worth noting that the long $Er_{Ba}-O_1$ bond and short $Er_{Ba}-O_2$ bond exhibit significant differences, which is the chemical bonding origin of Er-induced local distortions along the ⟨001⟩ direction we have shown previously.

4. CONCLUSIONS

Aiming to understand the effect of structure and vacancies on the optoelectronic properties of Er-doped BCTZ, we designed and prepared 1 mol % Er-doped BCTZ ceramics by the solid-state method. Our DFT calculations manifest that Er mainly occupies the A site (replacing Ba or Ca) and partly occupies the B site (replacing Ti or Zr) in BCTZ, generating both V_c and V_o. Compared to those of pure BCTZ, Er-doped BCTZ include less vacancies. The experimental results show that tetragonal phase is dominant in the ceramics. Er doping can reduce the crystal symmetry (increase the c/a ratio), inhibit the grain growth, increase the density, vary the Curie temperature, regulate the ferroelectric and piezoelectric properties, and endow the BCTZ ceramics with the upconversion PL feature. Furthermore, the properties of Er-doped BCTZ strongly depend on the concentrations of V_c and V_o. The ceramics with more V_o exhibit lower upconversion emission intensities, shorter lifetimes of red emission, and smaller P_r, whereas the ceramics with more V_c possess higher emission intensities, longer PL lifetimes at 667 nm, lower T_c, and much higher d_{33} (reach up to 372 pC/N). The first-principles calculations unravel that chemical bonding characters are distinct for Er-doped BCTZ with various site substitutions of Er. The A-site doping of Er in BCTZ brings local distortions along the ⟨001⟩ direction, resulting in increasing the PL intensity and d_{33}. This work provides evidence that the optoelectronic properties of Er-doped BCTZ ceramics are closely related to the structure and intrinsic vacancies.

■ ASSOCIATED CONTENT

Supporting Information

The Supporting Information is available free of charge on the ACS Publications website at DOI: 10.1021/acsomega.9b01391.

Rietveld refinement; lattice parameters (a and c); tetragonality ratio (c/a); and elemental mapping of Ba, Ca, Ti, Zr, Er, and O for the BCTZ-Er-y (y = 0, Ba, Ca, Ti, Zr) ceramics (PDF)

■ AUTHOR INFORMATION

Corresponding Authors

*E-mail: wuxiao@fzu.edu.cn (X.W.).
*E-mail: bssa@fzu.edu.cn (B.S.).

ORCID

Baisheng Sa: 0000-0002-9455-7795
Hailing Sun: 0000-0002-7292-4611
Laihui Luo: 0000-0002-2370-8277
Tengfei Lin: 0000-0001-7428-9829
Zhimei Sun: 0000-0002-4438-5032

Author Contributions

The manuscript was written through contributions of all authors. All authors have given approval to the final version of the manuscript.

Notes

The authors declare no competing financial interest.

■ ACKNOWLEDGMENTS

This work was supported by the National Key Research and Development Program of China (No. 2017YFB0701700), the National Natural Science Foundation of China (Nos. 51602055 and 61504028), the Key Laboratory of Eco-materials Advanced Technology (Fuzhou University), Fujian Province University (No. STHJ-KF1712), the "Qishan Scholar" Scientific Research Startup Project of Fuzhou University (No. XRC-1626), and the Testing Funding of Fuzhou University (No. 2017T004).

DOI: 10.1021/acsomega.9b01391
ACS Omega 2019, 4, 11004−11013

REFERENCES

(1) Peng, D.; Wang, X.; Xu, C.; Yao, X.; Lin, J.; Sun, T.; Nino, J. Bright Upconversion Emission, Increased T_c, Enhanced Ferroelectric and Piezoelectric Properties in Er-Doped $CaBi_4Ti_4O_{15}$ Multifunctional Ferroelectric Oxides. *J. Am. Ceram. Soc.* **2013**, *96*, 184−190.

(2) Kreisel, J.; Alexe, M.; Thomas, P. A. A Photoferroelectric Material is More than the Sum of its Parts. *Nat. Mater.* **2012**, *11*, 260−269.

(3) Lu, H.; Bark, C. W.; Esque, O. D.; Alcala, J.; Eom, C. B.; Catalan, G.; Gruverman, A. Mechanical Writing of Ferroelectric Polarization. *Science* **2012**, *336*, 59−68.

(4) Chen, G.; Ohulchanskyy, T. Y.; Kachynski, A.; Agren, H.; Prasad, P. N. Intense Visible and Near-Infrared Upconversion Photoluminescence in Colloidal $LiYF_4:Er^{3+}$ Nanocrystals under Excitation at 1490 nm. *ACS Nano* **2011**, *5*, 4981−4989.

(5) Deng, C. G.; He, C. J.; Sai, Q. L.; Liu, Y. W.; Xia, C. T.; Gu, X. R. Performance enhancement of white LED with TAG-Al_2O_3:Ce eutectic phosphor by partial Gd ion substitution. *Optik* **2018**, *160*, 176−181.

(6) Sun, H.; Peng, D.; Wang, X.; Tang, M.; Zhang, Q.; Yao, X. Strong Red Emission in Pr Doped $(Bi_{0.5}Na_{0.5})TiO_3$ Ferroelectric Ceramics. *J. Appl. Phys.* **2011**, *110*, No. 016102.

(7) Schlaghecken, G.; Gottmann, J.; Kreutz, E. W.; Poprawe, R. Pulsed Laser Deposition of Er:$BaTiO_3$ for Planar Waveguides. *Appl. Phys. A* **2004**, *79*, 1255−1257.

(8) Wu, X.; Kwok, K. W. Mid-IR to Visible Photoluminescence, Dielectric, and Ferroelectric Properties of Er-Doped KNLN Ceramics. *J. Am. Ceram. Soc.* **2014**, *97*, 1504−1510.

(9) Liu, W.; Ren, X. Large Piezoelectric Effect in Pb-Free Ceramics. *Phys. Rev. Lett.* **2009**, *103*, No. 257602.

(10) Zhao, C.; Wang, H.; Xiong, J.; Wu, J. Composition-Driven Phase Boundary and Electrical Properties in $Ba_{0.94}Ca_{0.06}Ti_{1-x}M_xO_3$ (M = Sn, Hf, Zr) Lead-Free Ceramics. *Dalton Trans.* **2016**, *45*, 6466−6480.

(11) Du, P.; Luo, L.; Li, W.; Yue, Q.; Chen, H. Optical Temperature Sensor Based on Upconversion Emission in Er-doped Ferroelectric $0.5Ba(Zr_{0.2}Ti_{0.8})O_3$-$0.5(Ba_{0.7}Ca_{0.3})TiO_3$ Ceramic. *Appl. Phys. Lett.* **2014**, *104*, No. 152902.

(12) Gong, S.; Ren, Z.; Jiang, S.; Li, M.; Li, X.; Wei, X.; Xu, G.; Shen, G.; Han, G. Phase-Modified Up-Conversion Luminescence in Er-Doped Single-Crystal $PbTiO_3$ Nanofibers. *J. Phys. Chem. C* **2014**, *118*, 5486−5493.

(13) Cohen, R. E. Origin of Ferroelectricity in Oxide Ferroelectrics and the Difference in Ferroelectric Behavior of $BaTiO_3$ and $PbTiO_3$. *Nature* **1992**, *136*, 95−103.

(14) Miao, N.; Bristowe, N. C.; Xu, B.; Verstraete, M. J.; Ghosez, P. First-Principles Study of the Lattice Dynamical Properties of Strontium Ruthenate. *J. Phys.: Condens. Matter* **2014**, *26*, No. 035401.

(15) Zhong, Z.; Wallerberger, M.; Tomczak, J. M.; Taranto, C.; Parragh, N.; Toschi, A.; Sangiovanni, G.; Held, K. Electronics with Correlated Oxides: $SrVO_3/SrTiO_3$ as a Mott Transistor. *Phys. Rev. Lett.* **2015**, *114*, No. 246401.

(16) Keeble, D. J.; Wicklein, S.; Dittmann, R.; Ravelli, L.; Mackie, R. A.; Egger, W. Identification of A- and B-site Cation Vacancy Defects in Perovskite Oxide Thin Films. *Phys. Rev. Lett.* **2010**, *105*, No. 226102.

(17) Hacene, M.; Anciaux-Sedrakian, A.; Rozanska, X.; Klahr, D.; Guignon, T.; Fleurat-Lessard, P. Accelerating VASP Electronic Structure Calculations Using Graphic Processing Units. *J. Comput. Chem.* **2012**, *33*, 2581−2589.

(18) Hutchinson, M.; Widom, M. VASP on A GPU: Application to Exact-Exchange Calculations of the Stability of Elemental Boron. *Comput. Phys. Commun.* **2012**, *183*, 1422−1426.

(19) Perdew, J. P.; Wang, Y. Accurate and Simple Analytic Representation of the Electron-Gas Correlation Energy. *Phys. Rev. B* **1992**, *45*, 13244−13249.

(20) Perdew, J. P.; Burke, K.; Wang, Y. Generalized Gradient Approximation for the Exchange-Correlation Hole of a Many-Electron System. *Phys. Rev. B* **1996**, *54*, 16533−16539.

(21) Momma, K.; Izumi, F. VESTA 3 for Three-Dimensional Visualization of Crystal, Volumetric and Morphology Data. *J. Appl. Crystallogr.* **2011**, *44*, 1272−1276.

(22) Zunger, A.; Wei, S.; Ferreira, L. G.; Bernard, J. E. Special Quasirandom Structures. *Phys. Rev. Lett.* **1990**, *65*, 353−356.

(23) Sun, Z.; Pan, Y.; Zhou, J.; Sa, B.; Ahuja, R. Origin of P-Type Conductivity in Layered $nGeTe{\cdot}mSb_2Te_3$ Chalcogenide Semiconductors. *Phys. Rev. B* **2011**, 83−93.

(24) Bai, Y.; Matousek, A.; Tofel, P.; Bijalwan, V.; Nan, B.; Hughes, H.; Button, T. W. $(Ba,Ca)(Zr,Ti)O_3$ Lead-Free Piezoelectric Ceramics - The Critical Role of Processing on Properties. *J. Eur. Ceram. Soc.* **2015**, *35*, 3445−3456.

(25) Sa, B.; Li, Y. L.; Qi, J.; Ahuja, R.; Sun, Z. Strain Engineering for Phosphorene: The Potential Application as a Photocatalyst. *J. Phys. Chem. C* **2014**, *118*, 26560−26568.

(26) Joshi, U. A.; Yoon, S.; Baik, S.; Lee, J. S. Surfactant-Free Hydrothermal Synthesis of Highly Tetragonal Barium Titanate Nanowires: A Structural Investigation. *J. Phys. Chem. B* **2006**, *110*, 12249−12256.

(27) Venkateswaran, U. D.; Naik, V. M.; Naik, R. High-Pressure Raman Studies of Polycrystalline $BaTiO_3$. *Phys. Rev. B* **1998**, *58*, 14256−14260.

(28) Gajović, A.; Plestina, J. V.; Zagar, K.; Plodinec, M.; Sturm, S.; Ceh, M. Temperature-Dependent Raman Spectroscopy of $BaTiO_3$ Nanorods Synthesized by Using a Template-Assisted Sol-Gel Procedure. *J. Raman Spectrosc.* **2013**, *44*, 412−420.

(29) Feteira, A.; Sinclair, D. C.; Kreisel, J. Average and Local Structure of $(1\text{-}x)BaTiO_3$-$xLaYO_3$ ($0 \leq x \leq 0.50$) Ceramics. *J. Am. Ceram. Soc.* **2010**, *93*, 4174−4181.

(30) Farhi, R.; Marssi, M. E.; Simon, A.; Ravez, J. A Raman and Dielectric Study of Ferroelectric $Ba(Ti_{1-x}Zr_x)O_3$ Ceramics. *Eur. Phys. J. B* **1999**, *9*, 599−604.

(31) Wu, X.; Kwok, K. W.; Li, F. Upconversion Fluorescence Studies of Sol-Gel-Derived Er-Doped KNN Ceramics. *J. Alloys Compd.* **2013**, *580*, 88−92.

(32) Miyayama, M.; Noguchi, Y. Polarization Properties and Oxygen-Vacancy Distribution of $SrBi_2Ta_2O_9$ Ceramics Modified by Ce and Pr. *J. Eur. Ceram. Soc.* **2005**, *25*, 2477−2482.

(33) He, C. J.; Sai, Q. L.; Xia, C. T.; Hu, H. L. Influence of Ce ion concentration on fluorescence properties of Ce:TAG-Al_2O_3 eutectic mixed crystals. *Cryst. Res. Technol.* **2017**, *52*, No. 1700056.

(34) Chen, L.; Liang, X.; Long, Z.; Wei, X. Upconversion Photoluminescence Properties of Er^{3+}-Doped $Ba_xSr_{1-x}TiO_3$ Powders with Different Phase Structure. *J. Alloys Compd.* **2012**, *516*, 49−52.

(35) Chai, X.; Li, J.; Wang, X.; Zhao, H.; Li, Y.; Yao, X. Dual-Mode Photoluminescence, Temperature Sensing and Enhanced Ferroelectric Properties in Er-Doped $(Ba_{0.4}Ca_{0.6})TiO_3$ Multifunctional Diphase Ceramics. *Mater. Sci. Eng., B* **2015**, *201*, 23−28.

(36) Zhang, Y.; Hao, J. H.; Mak, C. L.; Wei, X. H. Effects of Site Substitutions and Concentration on Upconversion Luminescence of Er^{3+}-Doped Perovskite Titanate. *Opt. Express* **2011**, *19*, 1824−1829.

(37) Chichibu, S. F.; Uedono, A.; Onuma, T.; DenBaars, S. P.; Mishra, U. K.; Speck, J. S.; Nakamura, S. Impact of Point Defects on the Luminescence Properties of (Al,Ga)N. *Mater. Sci. Forum* **2008**, *590*, 233−248.

(38) Chichibu, S. F.; Uedono, A.; Onuma, T.; Haskell, B. A.; Chakraborty, A.; Koyama, T.; Fini, P. T.; Keller, S.; Denbaars, S. P.; Speck, J. S.; Mishra, U. K.; Nakamura, S.; Yamaguchi, S.; Kamiyama, S.; Amano, H.; Akasaki, I.; Han, J.; Sota, T. Origin of Defect-Insensitive Emission Probability in In-Containing (Al,In,Ga)N Alloy Semiconductors. *Nat. Mater.* **2006**, *5*, 810−816.

(39) Lau, C. M.; Wu, X.; Kwok, K. W. Effects of Vacancies on Luminescence of Er-Doped $0.93Bi_{0.5}Na_{0.5}TiO_3$-$0.07BaTiO_3$ Ceramics. *J. Appl. Phys.* **2015**, *118*, No. 034107.

(40) Jo, W.; Granzow, T.; Aulbach, E.; Rödel, J.; Damjanovic, D. Origin of the Large Strain Response in $(K_{0.5}Na_{0.5})NbO_3$-Modified $(Bi_{0.5}Na_{0.5})TiO_3$-$BaTiO_3$ Lead-Free Piezoceramics. *J. Appl. Phys.* **2009**, *105*, No. 094102.

DOI: 10.1021/acsomega.9b01391
ACS Omega 2019, 4, 11004−11013

(41) Das, R. R.; Bhattacharya, P.; Perez, W.; Katiyar, R. S. Effect of Ca on Structural and Ferroelectric Properties of $SrBi_2Ta_2O_9$ and $SrBi_2Nb_2O_9$ Thin Films. *Ceram. Int.* **2004**, *30*, 1175−1179.
(42) Coondoo, I.; Panwar, N.; Amorín, H.; Ramana, V. E.; Alguero, M.; Kholkin, A.; Trolier-McKinstry, S. E.; et al. Enhanced Piezoelectric Properties of Praseodymium-Modified Lead-Free $(Ba_{0.85}Ca_{0.15})(Ti_{0.90}Zr_{0.10})O_3$ Ceramics. *J. Am. Ceram. Soc.* **2015**, *98*, 3127−3135.
(43) Noguchi, Y.; Miwa, I. G. Y.; Miyayama, M.; et al. Defect Control for Large Remanent Polarization in Bismuth Titanate Ferroelectrics Doping Effect of Higher-Valent Cations. *Jpn. J. Appl. Phys.* **2000**, *39*, L1259−L1262.
(44) Coondoo, I.; Agarwal, S. K.; Jha, A. K. Ferroelectric and Piezoelectric Properties of Tungsten Substituted $SrBi_2Ta_2O_9$ Ferroelectric Ceramics. *Mater. Res. Bull.* **2009**, *44*, 1288−1292.
(45) Takahashi, S.; Takahashi, M. Effects of Impurities on the Mechanical Quality Factor of Lead Zirconate Titanate Ceramics. *Jpn. J. Appl. Phys.* **1972**, *11*, 31−35.
(46) Silvi, B.; Savin, A. Classification of Chemical Bonds Based on Topological Analysis of Electron Localization Functions. *Nature* **1994**, *371*, 683−686.
(47) Sa, B.; Miao, N.; Sun, Z.; Wu, B. Polyhedral Transformation and Phase Transition in TcO_2. *RSC Adv.* **2015**, *5*, 1690−1696.
(48) Sa, B.; Zhou, J.; Sun, Z.; Tominaga, J.; Ahuja, R. Topological Insulating in $GeTe/Sb_2Te_3$ Phase-Change Superlattice. *Phys. Rev. Lett.* **2012**, *109*, No. 096802.

DOI: 10.1021/acsomega.9b01391
ACS Omega 2019, 4, 11004−11013